InSAR Imaging of Volcanic Deformation over Cloud-prone Areas – Aleutian Islands

Zhong Lu

Abstract

Interferometric synthetic aperture radar (INSAR) is capable of measuring ground-surface deformation with centimeter-to-subcentimeter precision and spatial resolution of tens-of-meters over a relatively large region. With its global coverage and all-weather imaging capability, INSAR is an important technique for measuring ground-surface deformation of volcanoes over cloud-prone and rainy regions such as the Aleutian Islands, where only less than 5 percent of optical imagery is usable due to inclement weather conditions. The spatial distribution of surface deformation data, derived from INSAR images, enables the construction of detailed mechanical models to enhance the study of magmatic processes. This paper reviews the basics of INSAR for volcanic deformation mapping and the INSAR studies of ten Aleutian volcanoes associated with both eruptive and non-eruptive activity. These studies demonstrate that all-weather INSAR imaging can improve our understanding of how the Aleutian volcanoes work and enhance our capability to predict future eruptions and associated hazards.

Principles of INSAR

Introduction

Interferometric synthetic aperture radar (INSAR) imaging is a recently developed remote sensing technique. The term "interferometry" draws its meaning from two root words: interfere and measure. The interaction of electromagnetic waves, referred to as interference, is used to measure precisely distances and angles. Interference of electromagnetic waves that are transmitted and received by synthetic aperture radar (SAR), an advanced imaging radar instrument, is called interferometric SAR (INSAR). Very simply, INSAR involves the use of two or more SAR images of the same area to extract the land surface topography and its deformation patterns.

INSAR is formed by interfering signals from two spatially or temporally separated antennas. The spatial separation of the two antennas is called the baseline. The two antennas may be mounted on a single platform for simultaneous interferometry, the usual implementation for aircraft and spaceborne systems such as Topographic SAR (TOPSAR) and Shuttle Radar Topography Mission (SRTM) systems (Zebker *et al.*, 1992; Farr and Kobrick, 2000). Alternatively, INSAR can be created by using a single antenna on an airborne or spaceborne platform in nearly identical repeating orbits for repeat-pass interferometry (Gray and Farris-Manning, 1993; Massonnet and Feigl, 1998). For the latter case, even though the antennas do not illuminate the same area at the same time, the two sets of signals recorded during the two passes will be highly correlated if the scattering properties of the ground surface remain undisturbed between viewings. This is the typical implementation for spaceborne sensors such as the U.S. SEASAT, European Remote-sensing Satellites (ERS-1 and ERS-2), Shuttle Imaging Radar-C (SIR-C), Canadian Radar Satellite (RADARSAT-1), Japanese Earth Resources Satellite (JERS-1), and European Environmental Satellite (ENVISAT), all of which operate at wavelengths ranging from a few centimeters (C-band) to tens of centimeters (L-band) (Table 1). This configuration makes INSAR capable of measuring ground-surface deformation with centimeter-to-subcentimeter precision at a spatial resolution of tens-of-meters over a relatively large region (approximately several 10^4 km^2).

The capability of measuring land surface deformation using repeat-pass INSAR data was first demonstrated by Gabriel *et al.* (1989). However, it was not until 1993 when Massonnet *et al.* (1993) published the discovery of mapping earthquake displacement from ERS-1 INSAR data that the science community enthusiastically began to embrace INSAR technology. Two years later, Massonnet *et al.* (1995) were also the first to apply ERS-1 INSAR imagery to map the volcanic deformation associated with the eruption of Etna Volcano. Today, scientists use INSAR data to study volcanoes worldwide. In this paper, I will briefly review the INSAR technique and discuss issues related to INSAR deformation mapping. I then present an overview of the use of INSAR to study volcanoes over cloud-prone and rainy regions, i.e., the Aleutian Islands.

Basics of INSAR

A SAR transmits electromagnetic waves at a wavelength ranging from a few millimeters to tens of centimeters. The radar wave propagates through the atmosphere and interacts with the Earth's surface. Part of the energy is returned back to and recorded by the SAR. Using a sophisticated image processing technique, called SAR processing (Curlander and McDonough, 1991; Bamler and Hartl, 1998; Henderson and Lewis, 1998), both the intensity and phase of the reflected (or backscattered) signal of each ground resolution element (a few meters to tens of meters) can be calculated in the form of a complex-valued SAR image representing the reflectivity of the ground surface. The amplitude or intensity of the SAR image (Plate 1a) is controlled primarily by terrain slope, surface roughness, and dielectric constants, whereas the phase of the SAR image (Plate 1b) is controlled primarily by the distance from satellite antenna to ground targets, the atmospheric delays, and the interaction of electromagnetic waves with ground surface.

A generation of an interferogram requires two single-look-complex (SLC) SAR images. Neglecting phase shifts

U.S. Geological Survey (USGS) Center for Earth Resources Observation and Science (EROS), 47914 252nd Street, Sioux Falls, SD, 57198 (lu@usgs.gov).

Photogrammetric Engineering & Remote Sensing
Vol. 73, No. 3, March 2007, pp. 245–257.

0099-1112/07/7303–0245/$3.00/0

TABLE 1. SPACEBORNE SAR SENSORS CAPABLE OF DEFORMATION MAPPING

Mission	Agency	Period of Operation	Orbit Repeat Cycle	Frequency	Wave-length	Incidence Angle at Swath Center	Resolution
SEASAT	NASA[2]	06/27 to 10/10, 1978	17 days	L-band 1.2 GHz	25 cm	20 to 26 degrees	25 m
ERS-1	ESA[3]	07/1991 to 03/2000	3, 168, and 35 days[4]	C-band 5.3 GHz	5.66 cm	23 degrees	30 m
SIR-C/X-SAR	NASA, DLR[5], and ASI[6]	04/09 to 04/20, 1994, and 09/30 to 10/11, 1994	6-month, 1-, 2-, 3-day[7] X-band 9.6 GHz	L-band 1.249 GHz C-band 5.298 GHz 3.1 cm	24.0 cm 5.66 cm	17 to 63 degrees (L- & C-band) 54 degrees (X-band)	10–200 m (30 m typical)
JERS-1	JAXA[8]	02/1992 to 10/1998	44 days	L-band 1.275 GHz	23.5 cm	39 degrees	20 m
ERS-2	ESA	04/1995 to present	35 days	C-band 5.3 GHz	5.66 cm	23 degrees	30 m
RADARSAT-1	CSA[9]	11/1995 to present	24 days	C-band 5.3 GHz	5.66 cm	10 to 60 degrees	10–100 m
ENVISAT	ESA	03/2002 to present	35 days	C-band 5.331 GHz	5.63 cm	15 to 45 degrees	20–100 m
ALOS	JAXA	01/2006 to present	46 days	L-band 1.270 GHz	23.6 cm	8 to 60 degrees	10–100 m
TERRASAR-X	DLR	Planned launch in late 2007	11 days	X-band 9.65 GHz	3.1 cm	20 to 55 degrees	1–16 m
RADARSAT-2	CSA	Planned launch in early 2007	24 days	C-band 5.405 GHz	5.55 cm	10 to 60 degrees	3–100 m

[1]Information was current in August 2006.
[2]National Aeronautics and Space Agency.
[3]European Space Agency.
[4]To accomplish various mission objectives, the ERS-1 repeat cycle was 3 days from 25 July 1991 to 01 April 1992, and from 23 December 1993, to 09 April 1994; 168 days from 10 April 1994 to 20 March 1995; and 35 days at other times.
[5]German Space Agency.
[6]Italian Space Agency.
[7]During days 3 to 4 of the second mission, SIR-C/X was commanded to retrace the flight path of the first mission to acquire repeat-pass INSAR data with a 6-month time separation. From day 7 to the end of the second flight, the shuttle was commanded to repeat the flight path of the previous days to acquire 1-day, 2-day, and 3-day repeat-pass INSAR data.
[8]Japan Aerospace Exploration Agency.
[9]Canadian Space Agency.

induced by the transmitting/receiving antenna and SAR processing algorithms, the phase value of a pixel in an SLC SAR image (Plate 1b) can be represented as

$$\phi_1 = -\frac{4\pi}{\lambda} r_1 + \varepsilon_1 \tag{1}$$

where r_1 is the apparent range distance (including possible atmospheric delay) from the antenna to the ground target, λ is the wavelength of radar, and ε_1 is the sum of phase shift due to the interaction between the incident radar wave and scatterers within the resolution cell. Because the backscattering phase (ε_1) is a randomly distributed (unknown) variable, the phase value (ϕ_1) in a single SAR image cannot be used to calculate the range (r_1) and is of no practical use. However, a second SLC SAR image (with the phase image shown in Plate 1c) could be obtained over the same area at a different time with a phase value of

$$\phi_2 = -\frac{4\pi}{\lambda} r_2 + \varepsilon_2. \tag{2}$$

Note that phase values in the second SAR image (Plate 1c) cannot provide range information (r_2) either.

An interferogram (Plate 1d) is created by co-registering two SAR images and differencing the corresponding phase values of the two SAR images (Plates 1b and 1c) on a pixel-by-pixel basis. The phase value of the resulting interferogram (Plate 1d) is

$$\phi = \phi_1 - \phi_2 = -\frac{4\pi(r_1 - r_2)}{\lambda} + (\varepsilon_1 - \varepsilon_2). \tag{3}$$

The fundamental assumption in repeat-pass INSAR is that the scattering characteristics of the ground surface remain undisturbed. The degree of changes in backscattering characteristics can be quantified by the interferometric coherence, which is discussed further in a later section. Assuming that the interactions between the radar waves and scatterers remain the same when the two SAR images were acquired (i.e., $\varepsilon_1 = \varepsilon_2$), the interferometric phase value can be expressed as

$$\phi = -\frac{4\pi(r_1 - r_2)}{\lambda}. \tag{4}$$

Nominal values for the range difference, $(r_1 - r_2)$, extend from a few meters to several hundred meters. The SAR wavelength (λ) is of the order of several centimeters. Because the measured interferometric phase value (ϕ) is modulated by 2π, ranging from $-\pi$ to π, there is an ambiguity of many cycles (i.e., numerous 2π values) in the interferometric phase value. Therefore, the phase value of a single pixel in an interferogram is of no practical use. However, the change in range difference, $\delta(r_1 - r_2)$, between two neighboring pixels that are a few meters apart is normally much smaller than the SAR wavelength. So the phase difference between two nearby pixels, $\delta\phi$, can be used to infer the range distance difference $(r_1 - r_2)$ to a sub-wavelength precision. This explains how INSAR uses the phase difference to infer the change in range distance to an accuracy of centimeters or millimeters.

The phase (or range distance difference) in the original interferogram represented by Equation 4 and exemplified by Plate 1d contains contributions from both the topography and any possible ground surface deformation. Therefore, the topographic

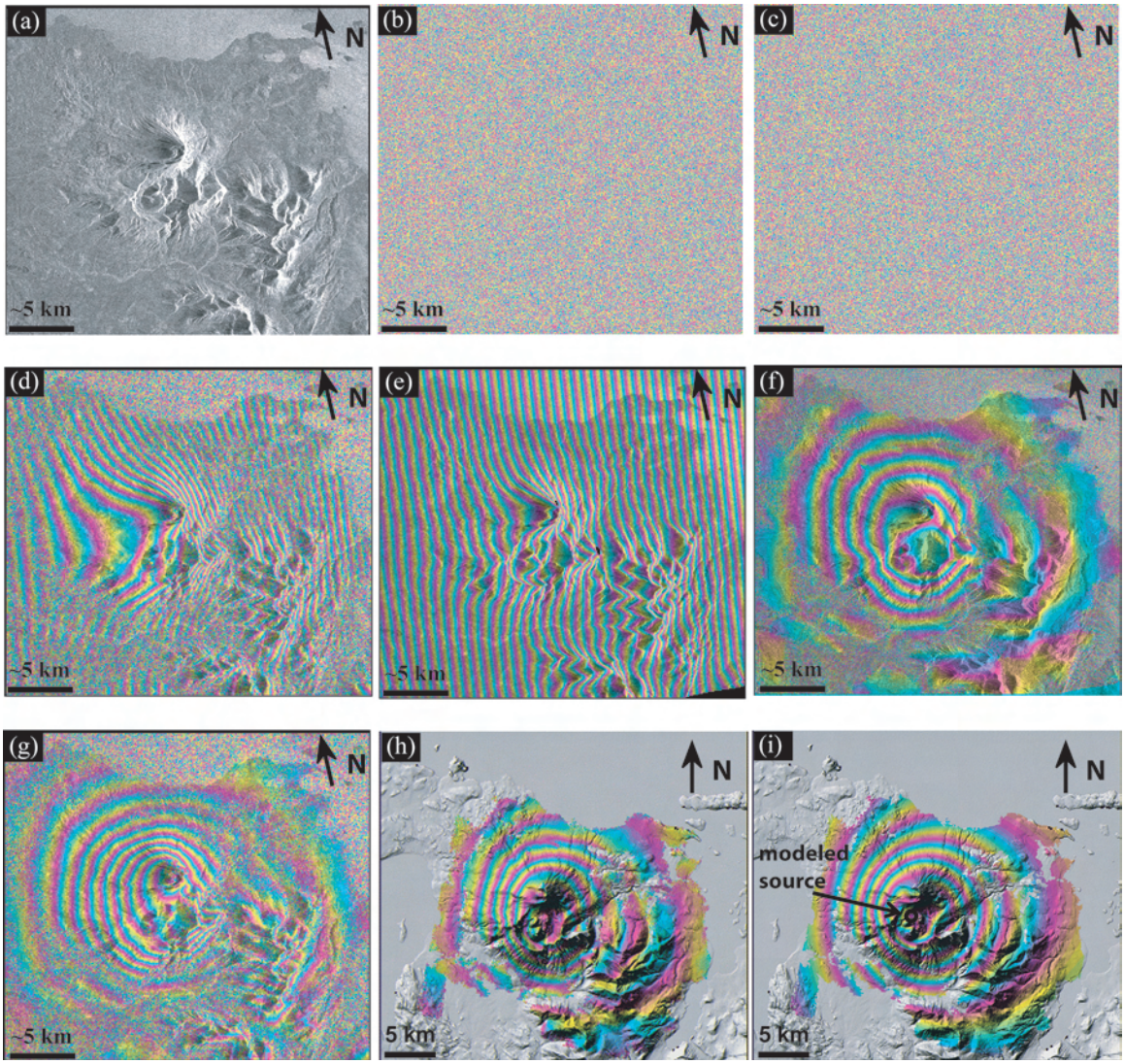

Plate 1. (a) The amplitude image of an SLC SAR image acquired on 04 October 1995 by the ERS-1 satellite over Peulik Volcano, Alaska. (b) The phase image of the SAR image acquired on 04 October 1995. (c) The phase image of an SLC SAR image acquired on 09 October 1997 by the ERS-2 satellite over Peulik Volcano, Alaska. The amplitude image is similar to that in Plate 1a and therefore is not shown. (d) An original interferogram formed by differencing the phase values of two co-registered SAR images (Plates 1b and 1c). The resulting interferogram contains fringes produced by the differing viewing geometries, topography, any atmospheric delays, and surface deformation. The perpendicular component of the baseline is 35 m. (e) An interferogram simulated to represent the topographic contribution in the original interferogram (Plate 1d). (f) A topography-removed interferogram that was produced by subtracting the interferogram in Plate 1e from the original interferogram in Plate 1d. (g) A flattened interferogram that was produced by removing the effect of an ellipsoidal earth surface from the original interferogram (Plate 1d). (h) A georeferenced interferogram overlaid on a shaded relief image produced from a DEM. The concentric pattern indicates approximately 17 cm of uplift centered on the southwest flank of Peulik Volcano, Alaska, which occurred during an aseismic inflation episode from October 1996 to September 1998 (Lu *et al.*, 2002b). (i) A modeled interferogram that was produced using a best-fit inflationary point source at about a 6.5 km depth with a volume change of 0.043 km^3 on the observed deformation image in Plate 1g. Each interferometric fringe (full-color cycle) represents 360° of phase change (or 2.83 cm of range change between the ground and the satellite). Areas of loss of radar coherence are uncolored in Plates 1h and 1i.

contribution needs to be removed from the original interferogram (Plate 1d) in order to derive a deformation map. The most common procedure is to use an existing digital elevation model (DEM) and the INSAR imaging geometry to produce a synthetic interferogram and subtract it from the interferogram to be studied (Massonnet and Feigl, 1998; Rosen *et al.*, 2000). This is the so-called 2-pass INSAR. Alternatively, the synthetic interferogram that represents the topographic contribution can come from a different interferogram of the same area. The procedures are then called 3-pass or 4-pass INSAR (Zebker *et al.*, 1994). As

the 2-pass INSAR method is commonly used in deformation mapping, a brief explanation of how to simulate the topographic effect based on an existing DEM follows.

Two steps are required to simulate a topography-only interferogram based on a DEM. First, the DEM needs to be resampled to project heights from a map coordinate into the appropriate radar geometry using geometric simulation of the imaging process. The INSAR imaging geometry is shown in Figure 1. The INSAR system acquires two images of the same scene with SAR platforms located at A_1 and A_2. The baseline, defined as the vector from A_1 to A_2, has a length B and is tilted with respect to the horizontal by an angle α. The slant range r from the SAR to a ground target T with an elevation value h is linearly related to the measured phase values in the SAR images by Equations 1 and 2. The look angle from A_1 to the ground point T is θ_1. For each ground resolution cell at ground range r_g with elevation h, the slant range value (r_1) should satisfy

$$r_1 = \sqrt{(H + R)^2 + (R + h)^2 - 2(H + R)(R + h)\cos\left(\frac{r_g}{R}\right)} \quad (5)$$

where H is the satellite altitude above a reference earth surface, which is assumed to be a sphere with radius R. The

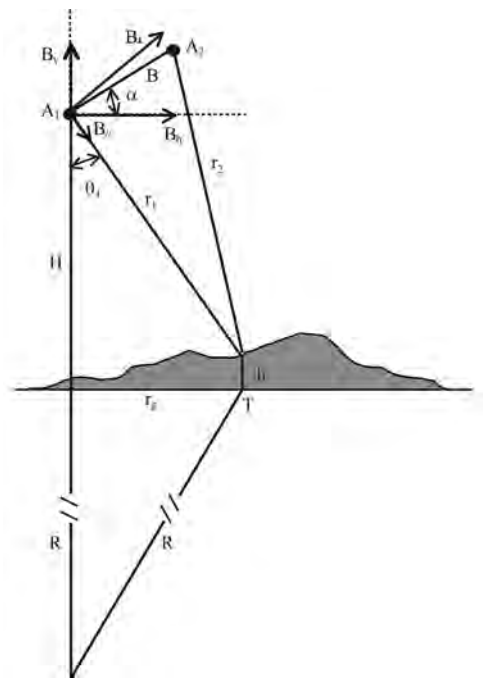

Figure 1. An INSAR imaging geometry. The INSAR system acquires two images of the same scene with SARs located at A_1 and A_2. The spatial distance between A_1 and A_2 is called the baseline, which has length B and is tilted with respect to the horizontal by α. The baseline B can be expressed by a pair of horizontal (B_h) and vertical (B_v) components, or a pair of parallel ($B_{//}$) and perpendicular$_\perp$(B) components. The range distances from the SARs to a ground target T with elevation h are r_1 and r_2, respectively. The look angle from A_1 to the ground point T is θ_1.

radar slant range and azimuth coordinates are calculated for each point in the DEM. This set of coordinates forms a non-uniformly sampled grid in the SAR coordinate space. The DEM height data are then resampled into a uniform grid in the radar coordinates using the values over the non-uniform grid.

Second, the precise look angle from A_1 to ground target T at ground range r_g, slant range r_1, and elevation h is calculated:

$$\theta_1 = \arccos\left[\frac{(H + R)^2 + r_1^2 - (R + h)^2}{2(H + R)r_1}\right]. \quad (6)$$

By knowing θ_1, the interferometric phase value due to the topographic effect at target T can be calculated,

$$\phi_{dem} = -\frac{4\pi}{\lambda}(r_1 - r_2)$$

$$= \frac{4\pi}{\lambda}\left(\sqrt{r_1^2 - 2(B_h \sin\theta_1 - B_v \cos\theta_1)\, r_1 + B^2} - r_1\right) \quad (7)$$

where B_h and B_v are horizontal and vertical components of the baseline B (Figure 1).

Plate 1e shows the simulated topographic effect in the interferogram in Plate 1d, using an existing DEM and the INSAR imaging geometry for the interferometric pair (Figure 1). Removing the topographic effects (Plate 1e) from the original interferogram (Plate 1d) results in an interferogram containing the ground surface deformation during the time duration and the measurement noise (Plate 1f) with the phase value given as

$$\phi_{def} = \phi - \phi_{dem}. \quad (8)$$

In practice, an ellipsoidal earth surface, characterized by its major axis, e_{maj}, and minor axis, e_{min}, is used to replace the spherical earth. The radius of the earth over the imaged area is then

$$R = \sqrt{(e_{min} \sin\beta)^2 + (e_{maj} \cos\beta)^2} \quad (9)$$

where β is the latitude of the center of the imaged region.

If h is taken as zero, the procedure outlined in Equations 5 through 9 will remove the effect of an ellipsoidal earth surface on the interferogram. This results in a flattened interferogram, where its phase value can be mathematically approximated as

$$\phi_{flat} = -\frac{4\pi}{\lambda}\frac{B\cos(\theta_1 - \alpha)}{r_1 \sin\theta_1} h + \phi_{def}$$

$$= -\frac{4\pi}{\lambda}\frac{B_\perp}{H \tan\theta_1} h + \phi_{def} \quad (10)$$

where $B_\perp$ is the perpendicular component of the baseline with respect to the incidence angle θ_1 (Figure 1). Removing the effect of an ellipsoidal earth surface on the original interferogram (Plate 1d) will result in a flattened interferogram (Plate 1g).

If ϕ_{def} is negligible in Equation 10, the phase value in Equation 10 can be used to calculate height h. This explains how INSAR can be used to produce an accurate, high-resolution DEM over a large region (Farr and Kobrick, 2000). For the ERS-1 and ERS-2 satellites, H is about 800 km, θ_1 is about 23° ± 3°, λ is 5.66 cm, and $B_\perp$ should be less than 1,100 m for a coherent interferogram. Therefore, Equation 10 can be approximated as

$$\phi_{flat} \approx -\frac{2\pi}{9600} B_\perp h + \phi_{def}. \quad (11)$$

For an interferogram with $B_\perp$ of 100 m, 1 m of topographic relief produces a phase value of about 4°. However, producing the same phase value requires only 0.3 mm of surface deformation. Therefore, it is evident that the interferogram phase value can be much more sensitive to changes in topography (i.e., the surface deformation ϕ_{def}) than to the topography itself (i.e., h). That explains why repeat-pass INSAR is capable of detecting surface deformation at a theoretical accuracy of sub-centimeters.

In the 2-pass INSAR deformation mapping, errors in the DEM can be mapped into deformation measurement. This is characterized by a term called the "altitude of ambiguity," which is the amount of topographic error required to generate one interferometric fringe in a topography-removed interferogram (Massonnet and Feigl, 1998). Because the altitude of ambiguity is inversely proportional to the baseline $B_\perp$, interferometric pairs with smaller baselines are better suited for deformation analysis.

The final procedure in 2-pass INSAR is to rectify the SAR images and interferograms into a map coordinate, which is a backward transformation of Equation 5. The georeferenced interferogram (Plate 1h) and derived products can be readily overlaid with other data layers to enhance the utility of the interferograms and facilitate data interpretation. Plate 1h shows six concentric fringes that represent about 17 cm of range decrease (mostly uplift) centered on the southwest flank of Peulik, Alaska. The volcano inflated aseismically from October 1996 to September 1998, a period that included an intense earthquake swarm that started in May 1998 over 30 km northwest of Peulik Volcano (Lu *et al.*, 2002b).

In-depth description of INSAR processing can be found in Rodriguez and Martin (1992), Zebker *et al.* (1994), Bamler and Hartl (1998), Henderson and Lewis (1998), Massonnet and Feigl (1998), Rosen *et al.* (2000), Zebker *et al.* (2000), Hensley *et al.* (2001), and Hanssen (2001). Interested readers should consult these references for further reading.

Interferogram Interpretation and Modeling

To understand volcanic processes, numerical models are often employed to invert the physical parameters based on the observed deformation. The spatial resolution of surface displacement data provided by INSAR makes it possible to constrain models of volcanic deformation with a variety of source geometries, such as the spherical point pressure source (Mogi source) (Mogi, 1958), the dislocation source (sill or dike source) (Okada, 1985), the ellipsoid source (Davis, 1986; Yang *et al.*, 1988), the penny-crack source (Fialko *et al.*, 2001). Among the physical parameters, location and volume change of the magma reservoir are the most important ones.

The most widely used source in volcano deformation modeling is the spherical point pressure source (also called the Mogi source) embedded in an elastic homogeneous half-space (Mogi, 1958). In a Cartesian coordinate system with the east, north, and up axes having an origin collocated with the upper-left (northwest) corner of an interferogram (Plate 1h), the predicted displacement (u) at the free surface of an elastic homogeneous half-space due to a change in the volume (ΔV) of a sphere (i.e., a presumed magma reservoir) is

$$u_i(x_1 - x'_1, x_2 - x'_2, 0) = \frac{(1 - v)(1 + v)}{2\pi(1 - 2v)} \frac{x_i - x'_i}{R^3} \Delta V \quad (12)$$

where x'_1, x'_2, and x'_3 are the horizontal locations and depth of the center of the sphere, R is the distance between the sphere and the location of observation (x_1, x_2, and 0), and v is the Poisson's ratio of the host rock. The four parameters used to describe the point source are horizontal location coordinates, depth, and volume change of a presumed magma body, which is calculated by assuming that the injected magma has the same elastic properties as the country rocks.

A nonlinear least-squares inversion approach is often used to optimize the source parameters in Equation 12 (Press *et al.*, 1992; Cervelli, 2001). Inverting the observed interferogram in Plate 1h using a Mogi source results in a best-fit source located at a depth of 6.5 $\pm$ 0.2 km. The calculated volume change is 0.043 $\pm$ 0.002 km^3. Plate 1i shows the modeled interferogram based on the best-fit source parameters. It is obvious that the Mogi source fits the observed deformation in Plate 1h very well.

Miscellaneous Issues in INSAR Processing

INSAR Coherence

Interferometric coherence is a qualitative assessment of the correlation of SAR images acquired at different times. It determines the amount of phase error and thus the accuracy of deformation estimates or DEM products. Constructing a coherent interferogram requires that SAR images must correlate with each other; that is, the backscattering spectrum must be substantially similar over the observation period. Physically, this translates into a requirement that the ground scattering surface be relatively undisturbed at the radar wavelength scale between measurements (Li and Goldstein, 1990; Zebker and Villasenor, 1992). Loss of INSAR coherence is also referred to decorrelation. There are three primary sources of decorrelation: (a) thermal decorrelation, caused by the presence of uncorrelated noise sources in radar instruments, (b) spatial decorrelation, which results when the target is viewed from different positions, and (c) temporal decorrelation, which is due to environmental changes such as vegetation and snow.

Reduction of radar coherence is the major obstacle to applying INSAR to Aleutian volcanoes. At these volcanoes, processes that reduce interferometric coherence include snow/ice melting and accumulation, freezing/thawing of surface material, erosion/deposition of volcanic lava and ash, and dense vegetation. Past studies have demonstrated that interferometric coherence at C-band is found to persist for three years or more on lava-flows and other rocky surfaces covered with short grass and sparsely distributed tall grass and for at least one year on most pyroclastic deposits (Lu and Freymueller, 1998; Lu *et al.*, 2002c). Interferometric coherence lasts for a few months on lava and rocky surfaces with dense tall grass, and on alluvium, coherence lasts for a few months. Snow and ice surfaces lose coherence within a few days. The comparison of L-band and C-band interferometric coherence at Aleutian volcanoes also suggests that L-band is far superior to C-band for studying volcanic surfaces covered with thick vegetation or loose material (Lu *et al.*, 2005a and 2005b). Therefore, chances for producing coherent interferograms are assured by using images acquired during summer or early fall, separated in time by a few months (in the same summer/fall) or one to a few years (Lu and Freymueller, 1998; Lu *et al.*, 2002c), and by using L-band imagery over surfaces with thick vegetation or loose material (Lu *et al.*, 2005a and 2005b).

INSAR Baseline

A significant error source in INSAR deformation mapping is the baseline uncertainty due to inaccurate determination of SAR antenna positions. For ERS-1, ERS-2, and ENVISAT satellites, the refined precision orbit data provided by the German Processing and Archiving Facility (D-PAF) (Massmann, 1995) or Delft University in the Netherlands (Scharroo and Visser, 1998) should be used for INSAR processing. The accuracy of the satellite position vectors provided in RADARSAT-1 and JERS-1 metadata is much poorer than that for ERS-1, ERS-2, and ENVISAT. Therefore, baseline refinement is particularly

required for RADARSAT-1 or JERS-1 interferogram processing. Even for ERS-1, ERS-2, and ENVISAT satellites where precise restitute vectors are available, baseline errors in interferograms can often be present. Plate 2a is an interferogram of Okmok Volcano from a pair of ERS-2 images acquired on 18 August 2000, and 19 July 2002. The precision position vectors are used for the INSAR processing. The apparent range changes due to baseline errors are obvious, and the volcanic deformation over the island can be easily confused as there are more than three fringes outside the 10 km wide caldera. Therefore, interferogram baselines should be refined for INSAR deformation mapping. A commonly used method is to determine the baseline vector based on an existing DEM using a least-squares approach (Rosen *et al.*, 1996). In this approach, areas of the interferogram that are used to refine the baseline should have negligible deformation or the deformation is known from an independent source. Assuming the deformation away from the caldera is insignicant in the interferogram in Plate 2a, the baseline for this interferogram can be refined. Plate 2b shows the deformation interferogram produced with the refined baseline for the interferogram shown in Plate 2a. Volcanic deformation of more than three fringes (about 8 to 10 cm inflation) over the island can be observed from this interferogram, and it now becomes obvious that most of the deformation occurred within the caldera (Plate 2b).

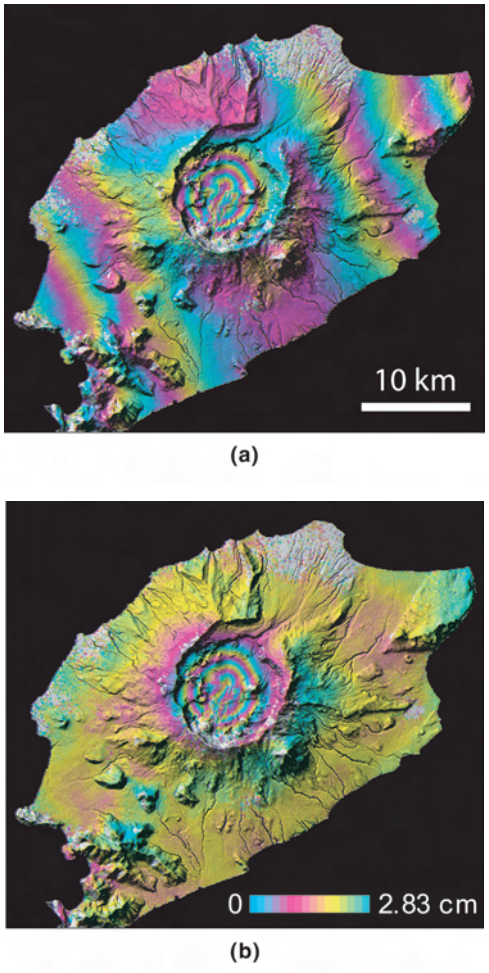

Plate 2. Topography-removed interferograms of Okmok Volcano (a) before and (b) after baseline refinement. Each interferometric fringe (full-color cycle) represents a 2.83 cm range change between the ground and the satellite.

Atmospheric Artifacts

Another significant error source in repeat-pass INSAR deformation measurement over cloud-prone and rainy areas is due to atmospheric delay anomalies caused by small variations in the index of refraction along the line of propagation. Spaceborne SAR sensors such as ERS-1, JERS-1, ERS-2, RADARSAT-1, and ENVISAT satellites orbit at altitudes of about 600 to 800 km. The electromagnetic wave from these sensors must propagate through the ionosphere, the stratosphere, and the troposphere. Therefore, the radar pulses are subject to small variations in the index of refraction along the line of propagation. Changes in temperature, pressure, and water vapor content of the atmosphere during the two observation instances will result in variations of phase of signals. These variations introduce errors in the observed interferogram. Zebker *et al.* (1997) indicated that variations of atmospheric water vapor contributed the most to atmospheric anomaly delays. Spatial and temporal changes of 20 percent in relative humidity could lead to 10 cm errors in repeat-pass interferometric deformation maps.

Over cloud-prone and rainy regions such as the Aleutian Islands, the range change caused by atmospheric delays can be significant. Plate 3a shows a topography-removed interferogram, covering the southeastern part of Okmok Volcano (Plate 2). This topography-removed interferogram is constructed using a pair of SAR images acquired in May and July 1997, respectively. Range change up to about 5 cm is observable. To confirm that the range changes in Plate 3a were caused by a difference in atmospheric conditions rather than by volcanic activity, another two interferograms were generated for the same area: one interferogram (Plate 3b) was produced using the image acquired in July 1997 (which was used in Plate 3a) and an image acquired in September 1997; the other interferogram (Plate 3c) was produced using the May and September 1997 images. In Plate 3b, apparent fringes similar to that in the May-July interferogram (Plate 3a) were observed. Because the change in color in Plate 3a is opposite that in Plate 3b, and because no fringe was observed in the May–September interferogram (Plate 3c), it is concluded that the fringes in Plate 3a and Plate 3b were most likely caused by an atmospheric anomaly that occurred primarily on the July 1997 image. Range changes of several centimeters have been found over other Aleutian volcanoes (e.g., Lu *et al.*, 2000c and 2003b). Therefore, multiple observations from independent interferograms for similar time intervals should be used to verify any apparent deformation (Zebker *et al.*, 1997; Lu *et al.*, 2000c). Because atmospheric artifacts do not correlate in time, stacking multiple interferograms will reduce atmospheric noise and enhance the signal-to-noise ratio of the deformation signal (Kwoun *et al.*, 2006).

INSAR Imaging of Aleutian Volcanoes

Introduction

Many volcanic eruptions are preceded by pronounced ground deformation in response to increasing pressure from magma chambers or to the upward intrusion of magma. Therefore, surface deformation patterns can provide important insights into the structure, plumbing, and state of restless volcanoes (Dvorak and Dzurisin, 1997; Dzurisin, 2003). By analogy with the earthquake cycle in seismology, an "eruption cycle" can be

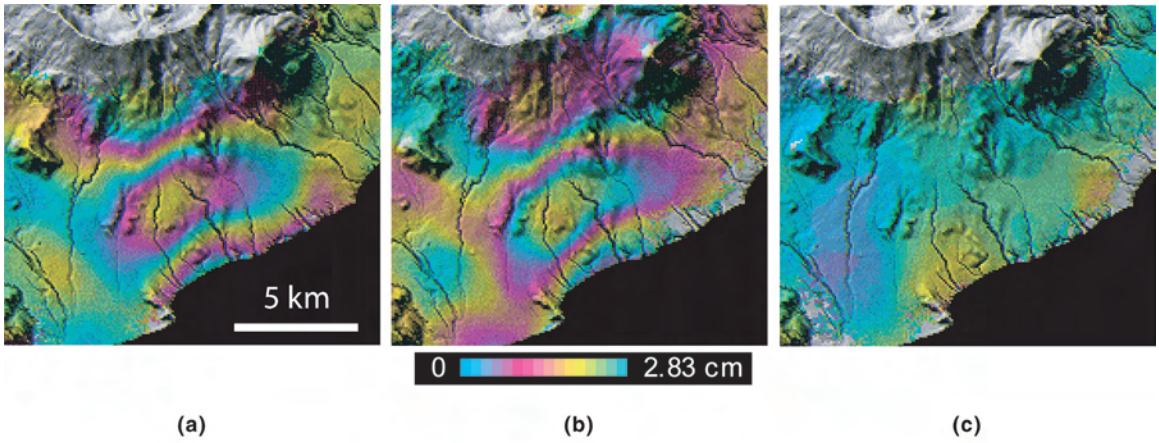

Plate 3. A portion of a topography-removed interferogram of Okmok Volcano shows severe atmospheric anomalies. (a) May to July 1997, (b) July to September 1997, and (c) May to September 1997.

conceptualized as a continuum from deep magma generation through surface eruption, including stages such as partial melting, initial ascent through the upper mantle and lower crust, crustal assimilation, magma mixing, degassing, shallow storage, and final ascent to the surface (Dzurisin, 2003). Not all stages are represented in every event. For example, some eruptions apparently are fed from shallow magma bodies that might not be replenished before every eruption, and others produce primitive lavas that show no evidence of storage, assimilation, or mixing. Some intrusions crystallize before they reach the surface and therefore might not advance the cycle toward the next eruption. The timescale for magma generation, ascent, and storage is poorly constrained and variable from one eruption to the next. In some cases, the

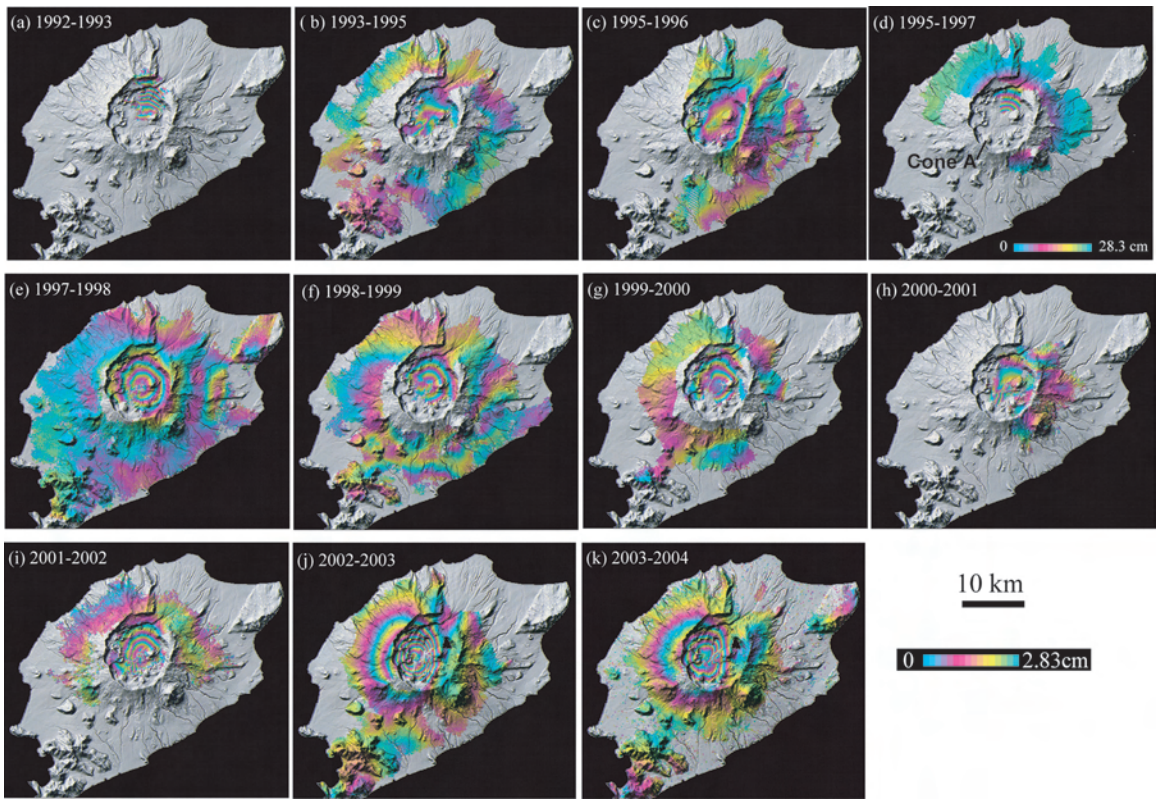

Plate 4. Deformation interferograms of Okmok Volcano for the periods (a, b, c) before, (d) during, and (e, f, g, h, i, j, k) after the February through April 1997 eruption. Areas of loss of radar coherence are uncolored. Unless otherwise noted, each interferometric fringe (full-color cycle) represents a 2.83 cm range change between the ground and the satellite.

early part of the cycle is relatively brief (e.g., rapid ascent of magma from a deep source directly to the surface), or the latter part is protracted (e.g., long periods of storage, assimilation, and crystallization between eruptions of large silicic caldera systems). As a result of such complexities, deformation patterns vary considerably both during the eruption cycle and between different volcanoes (Dvorak and Dzurisin, 1997). In addition, magma accumulations at shallow reservoirs typically occur below the brittle-ductile transition (approximately 5 km beneath volcanoes), so the slow ascent of magma to that depth is generally not marked by earthquakes (e.g., Sibson, 1982). Hence, the induced surface deformation is subtle, especially if the intrusion occurs episodically in a series of small events or gradually over a long time period. Therefore, understanding the dynamic processes of varied magma systems requires an imaging system capable of characterizing complex and dynamic volcano deformation patterns associated with different volcanic processes (Dzurisin, 2003). The chance for success in meeting this requirement has increased significantly since the recent advent of INSAR-aided volcano monitoring (e.g., Zebker *et al.*, 2000; Dzurisin, 2003; Lu *et al.*, 2003a; Pritchard and Simons, 2004).

The Aleutian volcanoes make up roughly ten percent of the world's active volcanoes. Major volcanic eruptions are annual events in the Aleutian arc. More than 170 eruptions were recorded in this area during the last 100 years. Although the rate of eruptive activities in the Aleutian arc is very high, these volcanoes remain relatively poorly studied due to their remote location, difficult logistics, and high cost of field measurement. Furthermore, nearly persistent cloud cover precludes acquisition of useful optical satellite images for a particular time period. In the past 30 years, only a few cloud-free optical images have been acquired for most of the Aleutian volcanoes (**http://glovis.usgs.gov**). Therefore, all-weather radar satellite images with the capability of measuring subtle ground surface deformation can significantly improve our understanding of activity at these volcanoes. The following sections summarize the investigation of Aleutian volcanoes with SAR images acquired from European ERS-1 and ERS-2, Canadian RADARSAT-1, and Japanese JERS-1 satellites: the INSAR studies for Okmok and Akutan Volcanoes will be elaborated in more detail, while work on other volcanoes will be briefly summarized.

Okmok Volcano

Okmok Volcano, a broad shield topped with a 10 km wide caldera, produced blocky, basaltic flows during relatively large, effusive eruptions in 1945, 1958, and 1997 (Miller *et al.*, 1998). All these eruptions originated from Cone A, located on the southern edge of the caldera floor (Plate 4).

INSAR images constructed from ERS-1, ERS-2, and RADARSAT-1 SAR data depict volcanic deformation before, during, and after the February through April 1997 eruption (Plate 4). More than five fringes appear inside the caldera in the 1992 to 1993 interferogram (Plate 4a), but only two fringes appear in the 1993 to 1995 interferogram (Plate 4b). It can be inferred from these two interferograms that the center of the caldera rose more than 14 cm during 1992 to 1993 and about 6 cm during 1993 to 1995. The 1995 to 1996 interferogram (Plate 4c) indicates that the caldera subsided approximately 1 to 2 cm between 1.5 and 0.5 years before the 1997 eruption. Therefore, the pre-eruption inflation rate decreased with time during 1992 to 1995, and inflation stopped sometime during 1995 to 1996. More than 140 cm of surface deflation associated with the 1997 eruption can be inferred from the ERS interferogram (Plate 4d). The deflation presumably is due to the withdrawal of magma (Lu *et al.*, 1998, 2000c, and 2005a). Progressive post-eruptive inflation from 1997 to 2004 is shown in Plates 4e through 4k. The post-eruption inflation rate generally decreased with time during 1997 to 2001. However, the inflation rate increased again during 2001 to 2004 to a value greater than that during 1997 to 1998. The inflation rate during 2002 to 2003 is the highest observed since the 1997 eruption.

Based on the shape and radial pattern of the displacement field, Lu *et al.* (2005a) assumed that deformation was caused by a volume change in a spherical magma reservoir, and modeled the surface displacement field using a point source within a homogenous isotropic elastic half-space (Mogi, 1958). Point-source models indicate that a magma reservoir at a depth of 3.2 km below sea level, located beneath the center of the caldera and about 5 km northeast of the 1997 vent, is responsible for the observed volcano-wide deformation.

Based on the observed interferograms and modeling results, a volcano deformation system for Okmok Volcano can be proposed as follows. A magma reservoir beneath the center of the caldera, about 3 km below sea level, was responsible for volcano-wide deformation before, during, and after the eruption. Magma filled this reservoir at a rate that varied both before and after the eruption, causing volcano-wide inflation. When the magma pressure within the reservoir reached a certain threshold, an eruption ensued. Withdrawal of magma as a result of an eruption depressurized the reservoir, causing volcano-wide deflation, and fed surface lava flows. Magma started to accumulate in the reservoir soon after the eruption stopped, initiating a new inter-eruption strain cycle. By the summer of 2004, approximately 40 to 70 percent of the magma volume lost from the reservoir in the 1997 eruption had been replenished. This case study for Okmok Volcano has demonstrated that INSAR is capable of measuring pre-eruptive, co-eruptive, and post-eruptive deformation in the sub-arctic, cloud-prone environment (Lu *et al.*, 1998, 2000c, 2003c, and 2005a).

Akutan Volcano

Akutan Volcano, the second most active volcano in the Aleutian arc with more than 27 eruptive episodes in the last two centuries, is located in the west-central part of Akutan Island in the eastern Aleutian volcanic arc. It is a composite stratovolcano with a circular summit caldera about 2 km across (Miller *et al.*, 1998) (Plate 5). Lava flows, pyroclastic flows, and other types of volcanic deposits cover much of the west portion of the island, including Akutan Volcano. The east half of the island, on the other hand, consists mainly of older, relatively loose deposits (tephra and ash) and undifferentiated volcanic rocks (Miller *et al.*, 1998). In general, vegetation is denser on the east half of the island than on the west half (Plate 5).

Akutan Island was shaken in March 1996 by an intense earthquake swarm accompanied by extensive ground cracking but with no eruption of the volcano. Fresh ground cracks were observed, and the most extensive cracks occurred in a zone roughly 500 m wide and 3 km long between Lava Point and the summit of Akutan Volcano. Two deformation interferograms that bracket the March 1996 swarm are shown in Plate 5. The interferogram in Plate 5a was produced from C-band (wavelength = 5.66 cm) ERS images acquired on 20 August 1993, and 07 October 1996, whereas the interferogram in Plate 5b is an L-band (wavelength = 23.5 cm) JERS-1 deformation interferogram that spans the time interval from 28 October 1994, to 22 June 1997. It is obvious that interferometric coherence is significantly higher at L-band than at C-band over similar time intervals. Both the ERS and JERS-1 interferograms show that the western part of the island was uplifted about 60 cm during the 1996 seismic swarm. The JERS-1 interferogram (Plate 5c) also shows localized subsidence in the zone of intense ground cracking associated with the swarm on the northwest flank of Akutan

Volcano. The subsidence is not observable in the ERS interferograms, owing to loss of interferometric coherence. Wholesale uplift of the volcanic edifice, combined with localized ground cracking, has been attributed to magma accumulation and intrusion at other volcanoes (e.g., Rubin, 1992). In addition, the JERS-1 interferogram reveals displacement on two normal faults that were re-activated during the 1996 seismic swarm (Plates 5d and 5e). Displacement profiles across the faults show that the magnitude of displacement was about 5 cm (Plates 5d and 5e), which is consistent with the observed ground breakage of several centimeters (Richter *et al.*, 1998).

The complexity of the deformation field revealed by the interferograms makes it difficult to identify a unique model for the deformation sources. Lu *et al.* (2000b and 2005b) explored a range of possible models using as constraints the asymmetric uplift of Akutan Volcano, the geometry of surface fractures on its northwest flank, and the orientation of reactivated faults on the eastern part of the island. The interferograms were modeled with elastic Mogi sources (Mogi, 1958) and dislocation sources (Okada, 1985). These models suggest that the top of the magma intruded to a depth of 1 km beneath the surface (Lu *et al.*, 2005b).

INSAR study of Akutan Volcano has demonstrated that L-band INSAR is far superior to C-band for studying volcanic surfaces covered with thick vegetation or loose material. The ability to map surface deformation at high spatial resolution with INSAR makes it an especially useful tool for studying complex deformation patterns, such as those associated with the March 1996 seismic swarm at Akutan Island. In addition, interferograms in Plates 5a and 5b provide a rare glimpse of surface deformation associated with magma intrusion beneath an island arc volcano. Such effects are often obscured by subsequent eruptive activity, including syn- and post-eruption deformation that might not be distinguishable from pre-eruption effects. This example demonstrates that INSAR can provide a basis not only for interpreting and modeling movement of shallow magma bodies that feed eruptions, but also for detecting intrusive activities that do not result in an eruption (Lu *et al.*, 2000a and 2005b). The two-dimensional imaging capability of INSAR facilitates characterizing the complex deformation field at Akutan Volcano, and thereby improves our understanding of its dynamics.

Augustine Volcano

Augustine Volcano, an 8 km by 11 km island, underwent six significant eruptions in the last two centuries: 1812, 1883, 1935, 1963 to 1964, 1976, and 1986. INSAR images show that the pyroclastic flows from the 1986 eruption have been experiencing subsidence/compaction at a rate of about 3 cm per year (Plate 6a), but no sign of significant volcano-wide deformation was observed during 1992 to 2000. The observed deformation can be used to study the characteristics of the pyroclastic flows (Lu *et al.*, 2003a).

Peulik Volcano

Peulik Volcano, a stratovolcano located on the Alaska Peninsula, is known to have erupted in 1814 and 1852 (Miller *et al.*, 1998). INSAR images that collectively span the time interval from July 1992 to August 2000 reveal that a presumed magma body located 6.6 km beneath Peulik Volcano inflated 0.051 km^3 between October 1996 and September 1998. The average inflation rate of the magma body was about 0.003 km^3 per month from October 1996 to September 1997 (Plate 6b), peaking at 0.005 km^3 per month from 26 June to 09 October 1997, and dropping to 0.001 km^3 per month from October 1997 to September 1998. Deformation before October 1996 and after September 1998 was not significant. An intense earthquake swarm occurred about 30 km northwest of Peulik from May to October 1998, around the end of the inflation period. The 1996 to 1998 inflation episode at Peulik confirms that INSAR can be used to detect magma accumulation beneath dormant volcanoes at least several months before other signs of unrest are apparent. This application represents a first step toward understanding the eruption cycle at Peulik and other stratovolcanoes with characteristically long repose periods (Lu *et al.*, 2002b).

Aniakchak Volcano

INSAR images from 1992 through 2002 at Aniakchak Volcano reveal that its 10 km wide caldera subsides about 13 mm per yr (Plate 6c) (Kwoun *et al.*, 2006). The depth of the deformation source (approximately 4 km) suggests that the subsidence can be explained by cooling or degassing of a shallow magma body and/or reduction of the pore-fluid pressure of a cooling hydrothermal system. Ongoing deformation of the volcano detected by INSAR, in combination with magmatic gas output from at least one warm spring and infrequent, low-level bursts of seismicity below the caldera, indicate that the magmatic system is still active.

Shishaldin Volcano

Multiple INSAR images with time spans of one year or more show no significant volcanic deformation in coherent parts of the images before, during, or after the 1995 to 1996 and 1999 eruptions at Shishaldin Volcano, the third-most active volcano in the Aleutian arc (Plate 6d) (Lu *et al.*, 2003a; Moran *et al.*, 2006). These studies indicate that any pre-eruption inflation may be compensated by subsequent withdrawal of a roughly equivalent volume of magma (leaving no net deformation field), suggesting the magma intrusion and transport might occur relatively quickly. If this interpretation is correct, improved monitoring of this type of volcano also requires observations from continuous global positioning system (GPS) stations and seismometers.

Westdahl Volcano

Westdahl Volcano, a young glacier-clad shield volcano, was frequently active during the latter half of the 20th century with documented eruptions in 1964, 1978 to 1979, and 1991 to 1992 (Miller *et al.*, 1998; Lu *et al.*, 2004). The background level of seismic activity since the last eruption was generally low (about five $M < 3$ earthquakes per year). INSAR images from 1991 to 2000 show that Westdahl Volcano deflated during its 1991 to 1992 eruption and is re-inflating at a rate that could produce another eruption in the next several years (Plate 6e). The rates of post-eruptive inflation and co-eruptive deflation are approximated by exponential decay functions with time constants of about six years and a few days, respectively. This behavior is consistent with a deep, constant-pressure magma source connected to a shallow reservoir by a magma-filled conduit where the magma flow rate is governed by the pressure gradient between the deep source and the shallow reservoir. This example demonstrates that (a) INSAR is becoming the best tool available for detecting deep, aseismic magma accumulation by measuring broad, subtle deformation of the ground surface to identify restless volcanoes long before they become active and before seismic and other precursors emerge, and (b) multiple-temporal INSAR images enable construction of a virtual magma plumbing system that can be used to constrain models of magma accumulation in the shallow reservoir and shed light on the time window of the next eruption (Lu *et al.*, 2000b, 2003b, and 2004).

Makushin Volcano

Makushin Volcano, a broad, ice-capped, truncated stratovolcano, is one of the more active volcanoes in the Aleutians,

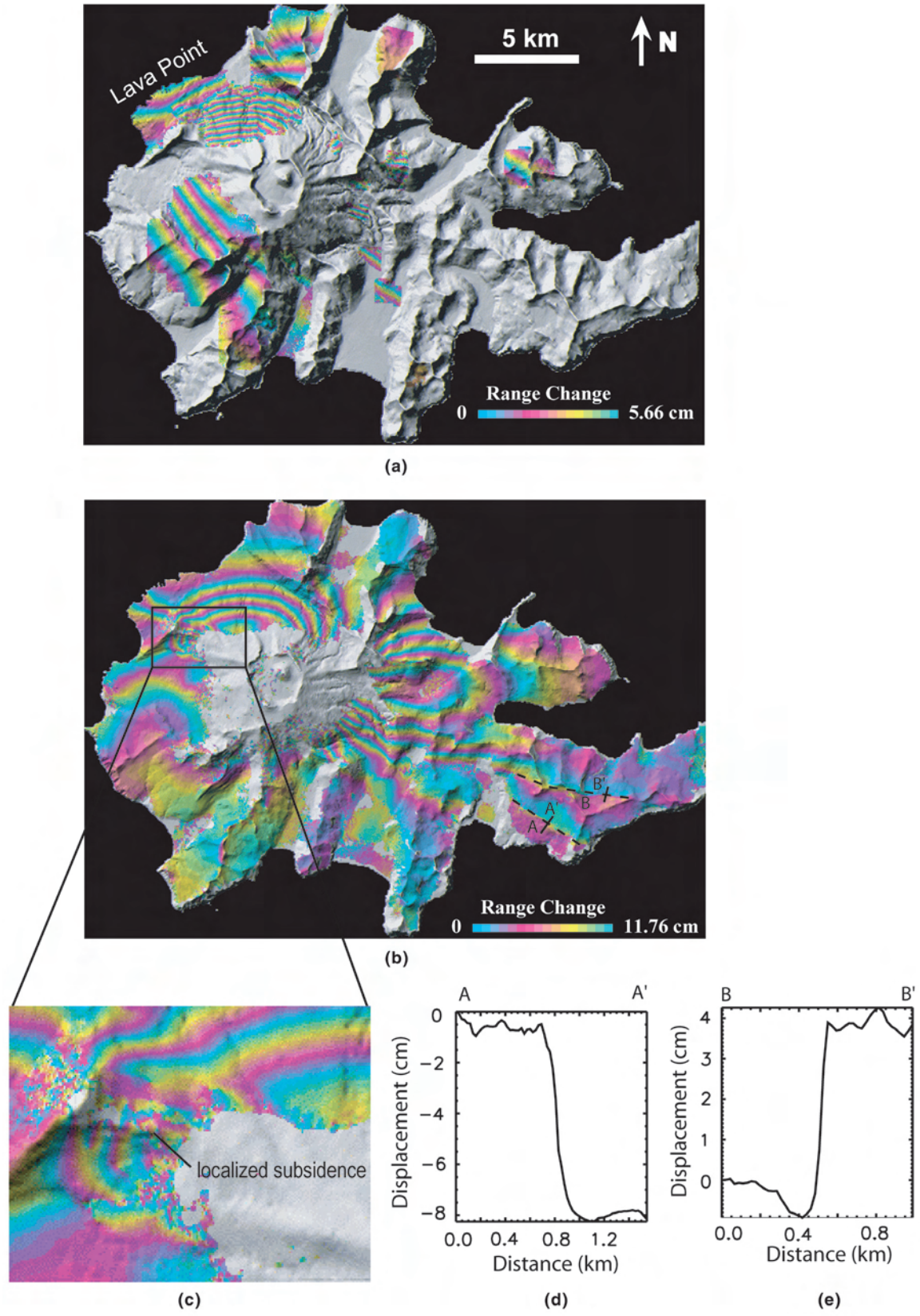

Plate 5. Deformation of Akutan Island during the 1996 seismic swarm mapped from (a) C-band ERS-1 and ERS-2 SAR images and (b) L-band JERS-1 SAR images, showing uplift of the west half of the island and subsidence of the east half. (c) Localized subsidence on the northwest flank of Akutan Volcano, where numerous ground cracks formed during the 1996 seismic swarm. (d, e) Deformation profiles across two faults that were activated during the March 1996 seismic swarm. Locations of the profiles are shown in (b).

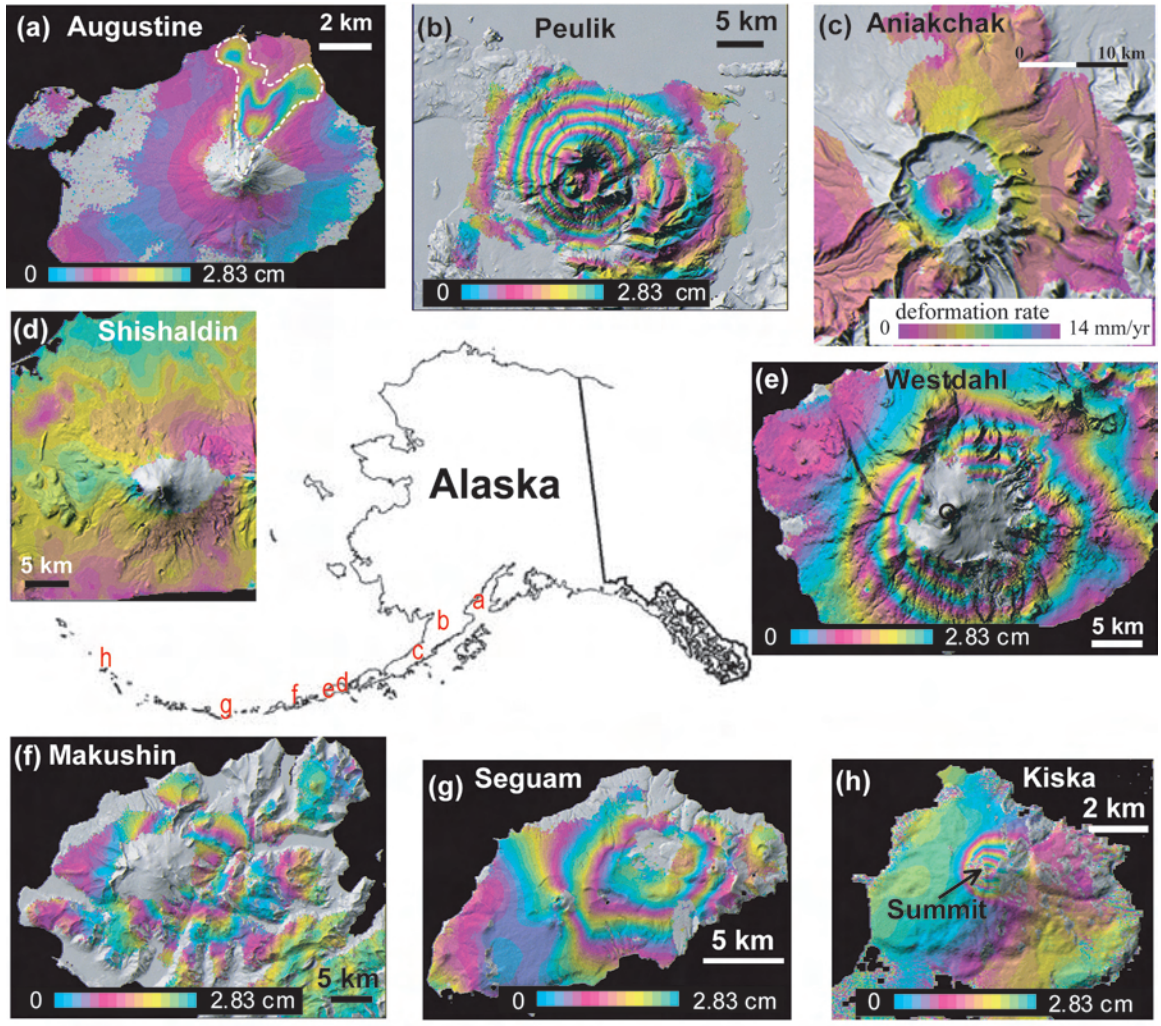

Plate 6. INSAR deformation images of selected volcanoes in the Aleutian Islands. (a) INSAR image (1992 to 1993) of Augustine Volcano that reveals deformation associated with compaction of 1986 pyroclastic flow deposits (outlined by white dashed line) (Lu *et al.*, 2003a). (b) INSAR image (1996 to 1997) showing approximately 17 cm of episodic uplift of Peulik Volcano (Lu *et al.*, 2002b). (c) An averaged INSAR image of Aniakchak Volcano showing that the caldera subsided about 13 mm per yr from 1992 to 2002 (Kwoun *et al.*, 2006). (d) INSAR image (1997 to 1999) of Shishaldin Volcano that shows no significant deformation associated with the volcano's 1999 eruption (Lu *et al.*, 2003a; Moran *et al.*, 2006). (e) INSAR image showing inflation of Westdahl Volcano during 1993 to 1998, which occurred aseismically (Lu *et al.*, 2000b and 2003b). The circle represents the horizontal position of an inferred shallow magma reservoir beneath Westdahl Peak. (f) INSAR image of Makushin Volcano showing about 7 cm of surface uplift associated with a possible eruption in January 1995 (Lu *et al.*, 2002c). (g) INSAR image of Seguam Volcano showing surface uplift of more than 6 cm during 1999 to 2000 (Lu *et al.*, 2003a; Masterlark and Lu, 2004). (h) INSAR image showing subsidence of Kiska Volcano during 1999 to 2000 (Lu *et al.*, 2002a) due to a change in the hydrothermal system. All interferograms are draped over DEM shaded relief images; areas without interferometric coherence are uncolored.

having produced at least 17 explosive, relatively small eruptions since the late 1700s (Miller *et al.*, 1998). Additional smaller eruptions probably occurred during this period but were unrecorded, either because they occurred when the volcano was obscured by clouds or because the eruptive products did not extend beyond the volcano's flanks. Several independent INSAR images, each spanning the time period from October 1993 to September 1995, show evidence of about 7 cm of uplift (Plate 6f) centered on the volcano's east flank. The uplift was interpreted as pre-eruptive inflation of a small explosive, but unsubstantially reported eruption on 30 January 1995. This example demonstrates that ground deformation of a few centimeters can be unambiguously identified with INSAR images over a rugged terrain where geometric distortion of radar images is severe (Lu et al., 2002c).

Seguam Volcano

Seguam Volcano, often referred to Pyre Peak, erupted in 1901, 1927, 1977, and 1992 to 1993 (Miller *et al.*, 1998). INSAR images, spanning various intervals from 1992 to

2000, document co-eruptive and post-eruptive deformation (Plate 6g) of the 1992 to 1993 eruption. A model that combines magma influx, thermoelastic relaxation, and poroelastic effects accounts for the observed deformation. This example demonstrates that spatial and temporal coverage of the INSAR data can be used to reveal dynamic processes within a volcano (Lu *et al.*, 2003a; Masterlark and Lu, 2004).

Kiska Volcano

Kiska Volcano is the westernmost, historically active volcano in the Aleutian arc. Sequential INSAR images of Kiska show a circular area, about 3 km in diameter and centered near the summit, that subsided by as much as 10 cm from 1995 to 2001, mostly during 1999 and 2000 (Plate 6h). Based on the shallow source depth (<1 km), the copious amounts of steam that were vented during recent eruptions, and recent field reports of vigorous steaming and persistent ground shaking near the summit area, the observed subsidence is attributed to decreased pore-fluid pressure within a shallow hydrothermal system beneath the summit area (Lu *et al.*, 2002a).

Conclusions

The satellite INSAR technique has proven to be a powerful space-borne geodetic tool for studying a variety of volcanic processes by analyzing surface deformation patterns (Lu *et al.*, 2005a and 2005b; 2004; 2003a, 2003b, and 2003c; 2002a, 2002b, and 2002c; 2000a, 2000b, and 2000c; 1998; 1997). The all-weather imaging capability of INSAR makes it an attractive tool for studying volcanic activity over cloud-prone environments. With the implementation of INSAR technology and growing INSAR-capable radar satellites (Table 1), volcano monitoring has entered an exciting phase wherein magma accumulation in the middle to upper crust can be observed long before the onset of short-term precursors to an eruption. Ultimately, more widespread use of INSAR for volcano monitoring could shed light on part of the eruption cycle, i.e., the time period between eruptions when a volcano seems to be doing essentially nothing. This makes INSAR an excellent space-based, long-term volcano monitoring tool. Combining applications of the INSAR technique with observations from continuous GPS, gravity, strainmeters, tiltmeters, seismometers, and volcanic gas studies will improve our capability to forecast future eruptions and will lead to improved volcano hazard assessment and better eruption preparedness.

Acknowledgments

ERS-1 and ERS-2, RADARSAT-1, and JERS-1 SAR images are copyrighted © 1991 through 2003 European Space Agency (ESA), 2000 to 2003 Canadian Space Agency (CSA), and 1992 through 1998 Japan Aerospace Exploration Agency (JAXA), respectively, and were provided by the Alaska Satellite Facility (ASF), JAXA, and ESA. The research summarized in this paper was supported by funding from the NASA RADARSAT/Cryosphere Program and the Solid Earth & Natural Hazards Program, the USGS Land Remote Sensing Program, and the USGS Volcano Hazards Program. I thank D. Dzurisin, C. Wicks, J. Power, J. Freymueller, O. Kwoun, D. Mann, T, Masterlark, V. McConnell, D. Meyer, S. Moran, R. Rykhus, W. Thatcher, and many other colleagues for their unselfish contributions to this research. I also thank the ASF, JAXA, and ESA staff members for their special efforts in making the SAR data available to us on a timely basis.

References

Bamler, R., and P. Hartl, 1998. Synthetic Aperture Radar Interferometry, *Inverse Problems*, 14:R1–54.

Cervelli, P., M.H. Murray, P. Segall, Y. Aoki, and T. Kato, 2001. Estimating source parameters from deformation data, with an application to the March 1997 earthquake swarm of the Izu Peninsula, Japan, *Journal of Geophysical Research*, 106:11,217–11,237.

Curlander, J., and R. McDonough, 1991. *Synthetic Aperture Radar Systems and Signal Processing*, New York, John Wiley & Sons.

Davis, P.M., 1986. Surface deformation due to inflation of an arbitrarily oriented triaxial ellipsoidal cavity in an elastic half-space, with reference to Kilauea Volcano, Hawaii, *Journal of Geophysical Research*, 91:7429–7438.

Dvorak, J., and D. Dzurisin, 1997. Volcano geodesy: The search for magma reservoirs and the formation of eruptive vents, *Review of Geophysics*, 35:343–384.

Dzurisin, D., 2003. A comprehensive approach to monitoring volcano deformation as a window on eruption cycle, *Review of Geophysics*, 41, doi:10.1029/2001RG000107.

Farr, T.G., and M. Kobrick, 2000. Shuttle Radar Topography Mission produces a wealth of data, *Eos Transactions*, 81:583–585.

Fialko, Y., Y. Khazan, and M. Simons, 2001. Deformation due to a pressurized horizontal circular crack in an elastic half-space, with applications to volcano geodesy, *Geophysical Journal International*, 146:181–190.

Gabriel, A.K., R.M. Goldstein, and H.A. Zebker, 1989. Mapping small elevation changes over large areas: Differential radar interferometry, *Journal of Geophysical Research*, 94:9183–9191.

Gray, A.L., and P.J. Farris-Manning, 2001. Repeat-pass interferometry with airborne synthetic aperture radar, *IEEE Transactions on Geoscience and Remote Sensing*, 31:180–191.

Hanssen, R., 2001. *Radar Interferometry: Data Interpretation and Error Analysis*, The Netherlands, Kluwer Academic Publishers.

Henderson, F., and A. Lewis, 1998. *Principals and Applications of Imaging Radar, Manual of Remote Sensing*, Vol. 2, John Wiley & Sons, Inc.

Hensley, S., R. Munjy, and P. Rosen, 2001. Interferometric Synthetic Aperture Radar (IFSAR), *Digital Elevation Model Technologies and Applications: The DEM Users Manual* (D.F. Maune, editor), American Society for Photogrammetry and Remote Sensing, pp. 143–206.

Kwoun, O., Z. Lu, C. Neal, and C. Wicks, 2006. Quiescent deformation of the Aniakchak Caldera, Alaska, mapped by InSAR, *Geology*, 30:5–8.

Li, F.K., and R.M. Goldstein, 1990. Studies of multibaseline spaceborne interferometric synthetic aperture radars, *IEEE Transactions on Geoscience and Remote Sensing*, 28:88–96.

Lu, Z., T. Masterlark, and D. Dzurisin, 2005a. Interferometric synthetic aperture radar (InSAR) study of Okmok Volcano, Alaska, 1992–2003: Magma supply dynamics and post-emplacement lava flow deformation, *Journal of Geophysical Research*, 110 (B2):B02403, doi:10.1029/2004JB003148.

Lu, Z., C. Wicks, O. Kwoun, J. Power, and D. Dzurisin, 2005b. Surface deformation associated with the March 1996 earthquake swarm at Akutan Island, Alaska, revealed by C-band ERS and L-band JERS radar interferometry, *Canadian Journal of Remote Sensing*, 31(1):7–20.

Lu, Z., R. Rykhus, T. Masterlark, and K. Dean, 2004. Mapping recent lava flows at Westdahl Volcano, Alaska, using radar and optical satellite imagery, *Remote Sensing of Environment*, 91:345–353.

Lu, Z., C. Wicks, D. Dzurisin, J. Power, W. Thatcher, and T. Masterlark, 2003a. Interferometric synthetic aperture radar studies of Alaska volcanoes, *Earth Observation Magazine (EOM)*, 12(3): 8–18.

Lu, Z., T. Masterlark, D. Dzurisin, R. Rykhus, and C. Wicks, 2003b. Magma supply dynamics at Westdahl Volcano, Alaska, Modeled from satellite radar interferometry, *Journal of Geophysical Research*, 108(B7), doi:10.1029/2002JB002311.

Lu, Z., E. Fielding, M. Patrick, and C. Trautwein, 2003c. Estimating lava volume by precision combination of multiple baseline spaceborne and airborne interferometric synthetic aperture radar: The 1997 eruption of Okmok Volcano, Alaska, *IEEE*

Transactions on Geoscience and Remote Sensing, 41(6): 1428–1436.

Lu, Z., T. Masterlark, J. Power, D. Dzurisin, and C. Wicks, 2002a. Subsidence at Kiska Volcano, Western Aleutians, detected by satellite radar interferometry, *Geophysical Research Letters*, 29(18):1855, doi:10.1029/2002GL014948.

Lu, Z., C. Wicks, D. Dzurisin J. Power, S. Moran, and W. Thatcher, 2002b. Magmatic inflation at a dormant stratovolcano: 1996–98 activity at Mount Peulik Volcano, Alaska, revealed by satellite radar interferometry, *Journal of Geophysical Research*, 107(B7): 2134, doi:10.1029/2001JB000471.

Lu, Z., J. Power, V. McConnell, C. Wicks, and D. Dzurisin, 2002c. Pre-eruptive inflation and surface interferometric coherence characteristics revealed by satellite radar interferometry at Makushin Volcano, Alaska: 1993–2000, *Journal of Geophysical Research*, 107(B11):2266, doi:10.1029/2001JB000970.

Lu, Z., C. Wicks, J. Power, and D. Dzurisin, 2000a. Ground deformation associated with the March 1996 earthquake swarm at Akutan Volcano, Alaska, revealed by satellite radar interferometry, *Journal of Geophysical Research*, 105:21,483–21,496.

Lu, Z., C. Wicks, D. Dzurisin, W. Thatcher, J. Freymueller, S. McNutt, and D. Mann, 2000b. Aseismic inflation of Westdahl Volcano, Alaska, revealed by satellite radar interferometry, *Geophysical Research Letters*, 27:1567–1570.

Lu, Z., D. Mann, J. Freymueller, and D. Meyer, 2000c. Synthetic aperture radar interferometry of Okmok Volcano, Alaska: Radar observations, *Journal of Geophysical Research*, 105:10791–10806.

Lu, Z., D. Mann, and J. Freymueller, 1998. Satellite radar interferometry measures deformation at Okmok Volcano, *EOS Transactions*, 79:461–468.

Lu, Z., and J. Freymueller, 1998. Synthetic aperture radar interferometry coherence analysis over Katmai Volcano Group, Alaska, *Journal of Geophysical Research*, 103:29887–29894.

Lu, Z., R. Fatland, M. Wyss, S. Li, J. Eichelberger, K. Dean, and J. Freymueller, 1997. Deformation of New Trident Volcano measured by ERS-1 SAR interferometry, Katmai National Park, Alaska, *Geophysical Research Letters*, 24:695–698.

Massmann, F.H., 1995. *Information for ERS PRL/PRC Users*, GeoForschungs Zentrum Potsdam Technical Note.

Massonnet, D., M. Rossi, C. Carmona, F. Adragna, G. Peltzer, K. Feigi, and T. Rabaute, 1993. The displacement field of the Landers earthquake mapped by radar interferometry, *Nature*, 364:138–142.

Massonnet, D., P. Briole, and A. Arnaud, 1995. Deflation of Mount Etna monitored by spaceborne radar interferometry, *Nature*, 375:567–570.

Massonnet, D., and K. Feigl, 1998. Radar interferometry and its application to changes in the Earth's surface, *Review of Geophysics*, 36:441–500.

Masterlark, T., and Z. Lu, 2004. Transient volcano deformation sources imaged with InSAR: Application to Seguam Island, *Journal of Geophysical Research*, 109:B01401, doi:10.1029/2003JB002568.

Moran, S., O. Kwoun, T. Masterlark, and Z. Lu, 2006. On the absence of deformation signals from InSAR interferograms bracketing the 1995–1996 and 1999 eruptions of Shishaldin Volcano, Alaska, *Journal of Volcanology and Geothermal Research*, 150:119–131.

Miller, T.M., R.G. McGimsey, D.H. Richter, J.R. Riehle, C.J. Nye, M.E. Yount, and J.A. Dumoulin, 1998. Catalog of the historically active volcanoes of Alaska, *USGS Open-File Report*, 98–582.

Mogi, K., 1958. Relations between the eruptions of various volcanoes and the deformations of the ground surface around them, *Bulletin of the Earthquake Research Institute*, University of Tokyo, 36:99–134.

Okada, Y., 1985. Surface deformation due to shear and tensile faults in a half-space, *Bulletin of the Seismological Society of America*, 75:1135–1154.

Press, W., S. Teukolsky, W. Vetterling, and B. Flannery, 1992. *Numerical Recipes in C, The Art of Scientific Computing*, Cambridge University Press, 994 p.

Pritchard, M., and M. Simons, 2004. Surveying volcanic arcs with satellite radar interferometry: The Central Andes, Kamchatka, and beyond, *Geological Society of America (GSA) Today*, 14(8): 4–11.

Richter, D.H., Waythomas, C.F., McGimsey, R.G., and Stelling, P.L. 1998. Geologic map of Akutan Island, Alaska, *USGS Open-File Report*, 98–135, 22 p.

Rosen, P., S. Hensley, H. Zebker, F.H. Webb, and E.J. Fielding, 1996. Surface deformation and coherence measurements of Kilauea Volcano, Hawaii, from SIR-C radar interferometry, *Journal of Geophysical Research*, 101:23109–23125.

Rosen, P., S. Hensley, I.R. Joughin, F.K. Li, S.N. Madsen, E. Rodriguez, and R.M. Goldstein, 2000. Synthetic aperture radar interferometry, *Proceedings of the IEEE*, 88:333–380.

Rubin, A.M. 1992. Dike-induced faulting and graben subsidence in the volcanic rift zones, *Journal of Geophysical Research*, 97: 1839–1858.

Scharroo, R., and P. Visser, 1998. Precise orbit determination and gravity filed improvement for the ERS satellites, *Journal of Geophysical Research*, 103(C4):8113–8127.

Sibson, R., 1982. Fault zone models, heat flow, and the depth distribution of seismicity in the continental crust of the United States, *Bulletin of the Seismological Society of America*, 72: 151–163.

Yang, X.-M., P.M. Davis, and J.H. Dieterich, 1988. Deformation from inflation of a dipping finite prolate spheroid in an elastic half-space as a model for volcanic stressing, *Journal of Geophysical Research*, 93:4249–4257.

Zebker, H.A., S.N. Madsen, and J. Martin, 1992. The TOPSAR interferometric radar topographic mapping instrument, *IEEE Transactions on Geoscience and Remote Sensing*, 30:933–940.

Zebker, H.A., and J. Villasenor, 1992. Decorrelation in Interferometric Radar Echoes, *IEEE Transactions on Geoscience and Remote Sensing*, 30:950–959.

Zebker, H.A., P.A. Rosen, R.M. Goldstein, A. Gabriel, and C.L. Werner, 1994. On the derivation of coseismic displacement fields using differential radar interferometry: The Landers earthquake, *Journal of Geophysical Research*, 99:19617–19634.

Zebker, H., P. Rosen, and S. Hensley, 1997. Atmospheric effects in interferometric synthetic aperture radar surface deformation and topographic maps, *Journal of Geophysical Research*, 102: 7547–7563.

Zebker, H., F. Amelung, and S. Jonsson, 2000. Remote sensing of volcano surface and internal processing using radar interferometry, *Remote Sensing of Active Volcanism*, AGU Monograph (P. Mouginis-Mark, editor), pp. 179–205.